

**THE INFLUENCE OF EQUAL CHANNEL ANGULAR PRESSING ANGLES
ON THE MICROSTRUCTURE AND PROPERTIES OF Al-Si-Mg ALLOY**

ALI ABADI ALTAYEF AL-JUBOURI

UNIVERSITI SAINS MALAYSIA

2006

**THE INFLUENCE OF EQUAL CHANNEL ANGULAR PRESSING ANGLES
ON THE MICROSTRUCTURE AND PROPERTIES OF Al-Si-Mg ALLOY**

by

ALI ABADI ALTAYEF AL-JUBOURI

**Thesis submitted in fulfillment of the
requirements for the degree
of Doctor of Philosophy**

July 2006

Dedicated to

*The dear memory of my late Parents with boundless
gratitude*

My darling wife Ibtisam, with my sincerest devotion

My loving brothers & sisters with my highest esteem

ACKNOWLEDGEMENTS

In the name of Allah, the most gracious and the most merciful and may his blessing be upon the prophet Mohamed (the blessings and peace of Allah be upon him). The great thanks to the great Almighty "ALLAH S.W" who grant me the health, knowledge, patience and the ability to complete this project.

I would like to sincerely express heartfelt gratitude to the invaluable assistance, guidance, and fruitful discussion of my supervisor, Associate professor Dr. Luay Bakir Hussain. I would like to express my deepest gratitude to my co-supervisor, Dr. Nurulakmal Mohammed Sharif for her help, guidance and support.

I'm grateful to Malaysian Government for offering me the honor of the MTCP scholarship, which reflects the high interest of the Government in higher education and scientific research. I would like to express my appreciation to the School of Materials and Mineral Resources Engineering, University Sains Malaysia for providing the necessary facilities for this project.

I would like to extend my grateful appreciation and thanks to Associate Professor Dr. Zulkifly Abdullah from the School of Mechanical Engineering (USM) for his assistance, helpful and providing his laboratory facilities for thermal conductivity measurements. My sincere thanks to Professor Hj Zainal Arifin Ahmad for providing the electrodes for corrosion experiments. I'm also thankful to Dr Sunara Purwadaria for his advice and answering my endless questions.

Special acknowledge is given to all academic, administrative and technical staff of the School of Material and Mineral Resources Engineering , Mr. Sharul Ami, Mr. Abd Rashid, Mrs. Hasnah, Mr. Hasnor, Miss. Mahani, Mr.

Helmi, Mr. Mokhtar, Mr. Suhaimi, Mr. Sayuti, Mr. Mohd Hasan, Mr. Azam, Mr. Faisal, Mr. Halim, Mr. Shahid, Mr. Kemuridan and Mrs. Fong. As well as , Mr. Abdul Latif , Mr. Amri and all technical staff of the School of Mechanical Engineering (USM) for their cooperative and friendly attitude that this research was carried out smoothly.

I would like to acknowledge the help provided by the Institute of Postgraduate Studies. Thanks to all staff of the library of the University Sains Malaysia.

My great thanks, compliments and regards to all my friends especially, Dr. Basil Qahtan, Ahmed Abu-foul, Kheder Al-jubouri, Yeoh Cheow Keat and all colleagues for help, kind accompaniment and support me in my effort.

Last, I would like to record a special word of thanks to my wife Ibtisam Gazi, for her endless support, patience and encouragement. I also wish to express my sincere thanks to my beloved brother and sisters along with my parents, brothers and sisters in laws and relatives who have giving me their unflinching support and encouragement.

TABLE OF CONTENTS

	Page
Dedication	i
Acknowledgement	ii
Table of Contents	iv
List of Tables	ix
List of Figures	xi
List of Symbols	xix
List of Abbreviations	xxi
List of Publications	xxii
Abstrak	xxiii
Abstract	xxv
CHAPTER ONE: INTRODUCTION	1
CHAPTER TWO : LITERATURE SURVEY	6
2.1 Aluminum and Aluminum Alloys	6
2.1.1 Aluminum and Aluminum Alloys Properties	6
2.1.2 Aluminum Series	8
2.2 Severe Plastic Deformation (SPD) Techniques	9
2.2.1 Multiple Forging (MF)	9
2.2.2 High Pressure Torsion (HPT)	10
2.2.3 Equal Channel Angular Pressing (ECAP)	13
2.3 Principle of ECAP	14

2.4	Estimations of the Strain in ECAP	18
2.5	Microstructure Evolution	19
2.5.1	Mechanism of Microstructural Evolution During ECAP	20
2.5.1(a)	Grains Subdivision	20
2.5.1(b)	Shearing Planes	25
2.5.1(c)	Deformation Texture	26
2.5.2	Strain effect on micrograin structure	28
2.6	Shearing Patterns	29
2.7	Microstructural developed by ECAP	31
2.7.1	The Effect of Die Channel	31
2.7.2	The Effect of Deformation Route	33
2.7.3	The Effect of Friction on the Deformation Homogeneity	35
2.8	Effect of ECAP on Materials Tensile	44
2.9	Submicrometer Grains and Hardness	46
2.10	ECAP in different materials	47
2.11	Thermal Conductivity	52
2.12	Corrosion Behavior	54
2.12.1	Corrosion of Ultra-fine Grained Materials	55
2.12.2	Corrosion Mechanism	58
2.12.3	Tafel's Equation	60
2.12.4	The Corrosion Rate	61
	CHAPTER THREE: MATERIALS AND METHODS	62
3.1	Material Composite	62

3.2	Mold Casting Preparation	62
3.3	Workpieces Preparation	64
3.3.1	Melting Aluminum Alloy	64
3.3.2	Heat Treatment of Al- alloy Workpieces	64
3.3.3	Workpieces Machining	66
3.4	Pressing Through ECAP Dies.	67
3.5	Scanning Electron Microscopy (SEM)	68
3.5.1	SEM Workpieces Preparation	69
3.6	Hardness Measurement	70
3.7	Tensile Test	72
3.8	Thermal Conductivity Measurement	74
3.9	Corrosion Test	75
	CHAPYER FOUR: RESULTS AND DISCUSIONS	77
4.1	Plastic Deformation Simulation	77
4.2	Al-Si-Mg Alloy ECAPed through a Die with $\Phi = 120^0$ and $\Psi = 0^0$	84
4.2.1	Microstructural Characteristics	84
4.2.2	Microhardness Measurements	86
4.2.3	The thermal Conductivity Measurements	89
4.3	Al-Si-Mg Alloy ECAPed through a Die with $\Phi = 90^0$ and $\Psi = 20^0$	92
4.3.1	Microstructural Characteristics	92
4.3.2	Micro hardness Measurements	96
4.3.3	The Thermal Conductivity Measurements	98
4.4	Annealed Al-Si-Mg Workpieces at 500^0C ECAPed through a Die with $\Phi = 90^0$ and $\Psi = 0^0$	102

4.4.1	Microstructural Characteristics	102
4.4.2	Microhardness Measurements	106
4.4.3	The Thermal Conductivity Measurements	109
4.5	Annealed Al-Si-Mg Workpieces at 600 °C ECAPed through a Die with $\Phi = 90^{\circ}$ and $\Psi = 20^{\circ}$	113
4.5.1	Microstructural Characteristics	113
4.5.2	Microhardness Measurements	118
4.5.3	The Thermal Conductivity Measurements	121
4.6	Tensile Test	125
4.7	Corrosion of Al-Si-Mg Alloy	134
4.7.1	The Influence of Microstructure on Corrosion	137
4.7.2	Corrosion Rate of ECAPed Al-Si-Mg Alloy Using a Die with $\Phi = 120^{\circ}$ and $\Psi = 0^{\circ}$	138
4.7.3	Corrosion Rate of ECAPed Al-Si-Mg alloy Using a Die with $\Phi = 90^{\circ}$ and $\Psi = 20^{\circ}$	142
4.7.4	Corrosion Rate of Annealed Al-Si-Mg Alloy at 500°C ECAPed Using a Die with $\Phi = 90^{\circ}$ and $\Psi = 0^{\circ}$	145
4.7.5	Corrosion Rate of Annealed Al-Si-Mg Alloy at 600 °C ECAPed Using a Die with $\Phi = 90^{\circ}$ and $\Psi = 20^{\circ}$	147
CHAPTER FIVE: CONCLUSIONS AND FUTURE SUGGESTIONS		154
5.1	Conclusions	154
5.2	Suggestion for Future Study	156
REFERENCES		157
APPENDICES		
APPENDIX A	Aluminum series and characteristics	171

APPENDIX B	Al-Mg phase diagram and Al-Si phase diagram	173
APPENDIX C	Thermal conductivity calculations using equation 2.12.	174
APPENDIX D	SEM photomicrographs showing microstructures of the Al-Si-Mg alloy; (a) after 1 pass on the Y-plane; (b) after 2 passes on the X-plane; (c) after 7 passes on Y-plane; (d) after 8 passes on Y-plane near the top edge of the workpiece.	175
APPENDIX E	Microstructures after ECAP using route B _C for (a) 3 passes at X-plane, (b) 5 passes at X-plane, (c) 6 passes at Y-plane, (d) 7 passes at X-plane.	177
APPENDIX F	Microstructures of annealed cast Al-Si-Mg alloy at 500 °C for 24h ECAPed using route B _C for (a) 1 pass on X-plane (b) 2 passes on Y-plane (c) 3 passes on X-plane (d) 6 passes on Y-plane.	179
APPENDIX G	Microstructures of cast and ECAPed Al-Si-Mg workpieces annealed at 600 °C for 30min at the first pass using route B _C followed by annealing at 230 °C for 20 min after 1 -3 passes (a) 2 pass in X- plane, (b) 3 passes on X- plane.	181
APPENDIX H	Polarization curves of ECAPed Al-Si-Mg alloy with various number of passed through a die with $\Phi=120^{\circ}$ and $\Psi=0^{\circ}$ after (a) 1 pass, (b) 2 passes, (c)3 passes, (d) 4 passes, (e)5 passes, and (f) 8 passes.	182
APPENDIX I	Polarization curves of ECAPed Al-Si-Mg alloy with various number of passed through a die with $\Phi=90^{\circ}$ and $\Psi=20^{\circ}$: (a) 2 passes, (b) 3 passes, (c) 4 passes, (d) 5 passes, (e) 6 passes, (f) 8 passes.	185
APPENDIX J	Polarization curves of ECAPed annealed Al-Si-Mg alloy at 500 °C for 24 h, after various number of passed through the die with $\Phi=90^{\circ}$ and $\Psi=0^{\circ}$: (a) 1 pass, (b) 2 passes, (c) 4 passes, (d) 5 passes, (e) 6 passes, and (f) 8 passes.	188
APPENDIX K	Polarization curves of ECAPed annealed Al-Si-Mg alloy at 600 °C for 30min at the first pass, with various number of passed through a die with $\Phi=90^{\circ}$ and $\Psi=20^{\circ}$: (a) 1 pass, (b) 2 passes annealed at 230 °C for 20 min, (c) 3 passes annealed at 230 °C for 20 min, and (d) 8 passes annealed at 230 °C for 30 min.	191

LIST OF TABLES

		Page
Table 2.1	Rotation angles and directions for six possible processing routes	35
Table 4.1	The temperature at all six sensor points installed at 10 mm intervals along the heater and heat sink sections with the number of passes of Al-Si-Mg workpieces through the die with $\Phi = 120^{\circ}$ and $\Psi = 0^{\circ}$	89
Table 4.2	The temperature at all six sensor points installed at 10 mm intervals along the heater and heat sink sections, also at the ends of the Al-Si-Mg workpieces with the number of passes of workpieces through the die with $\Phi = 120^{\circ}$ and $\Psi = 0^{\circ}$	89
Table 4.3	The temperature at all six sensor points installed at 10 mm intervals along the heater and heat sink sections with the number of passes of Al-Si-Mg workpieces through the die with $\Phi = 90^{\circ}$ and $\Psi = 20^{\circ}$	99
Table 4.4	The temperature at all six sensor points installed at 10 mm intervals along the heater and heat sink sections, also at the ends of the Al-Si-Mg workpieces with the number of passes of workpieces through the die with $\Phi = 90^{\circ}$ and $\Psi = 20^{\circ}$	99
Table 4.5	The temperature at all six sensor points installed at 10 mm intervals along the heater and heat sink sections with the number of passes of annealed Al-Si-Mg workpieces at 500°C for 24h through the die with $\Phi = 90^{\circ}$ and $\Psi = 0^{\circ}$	110
Table 4.6	The temperature at all six sensor points installed at 10 mm intervals along the heater and heat sink sections, also at the ends of the annealed Al-Si-Mg workpieces at 500°C for 24h with the number of passes of workpieces through the die with $\Phi = 90^{\circ}$ and $\Psi = 0^{\circ}$	110
Table 4.7	The temperature at all six sensor points installed at 10 mm intervals along the heater and heat sink sections with the number of passes of annealed Al-Si-Mg workpieces at 600°C for 30 min through the die with $\Phi = 90^{\circ}$ and $\Psi = 20^{\circ}$	121
Table 4.8	The temperature at all six sensor points installed at 10 mm intervals along the heater and heat sink sections, also at the ends of the annealed Al-Si-Mg workpieces at 600°C for 30 min with the number of passes of workpieces through the die with $\Phi = 90^{\circ}$ and $\Psi = 20^{\circ}$	121

Table 4.9	Corrosion rate of Al-Si-Mg workpieces with the number of passes through the ECAP die with $\Phi = 120^\circ$ and $\Psi = 0^\circ$.	139
Table 4.10	Corrosion rate of Al-Si-Mg workpieces with the number of passes through the ECAP die with $\Phi = 90^\circ$ and $\Psi = 20^\circ$	142
Table 4.11	Corrosion rate of annealed Al-Si-Mg workpieces at 500°C for 24h before ECAP with the number of passes through the die with $\Phi = 90^\circ$ and $\Psi = 0^\circ$	145
Table 4.12	Corrosion rate for none pressed and ECAPed Al-Si-Mg workpieces heat treated at 600°C for 30 min at first pass followed by annealing at 230°C for 20 min up to three passes and for 30 min at seven and eight passes	148

LIST OF FIGURES

		Page
Figure 2.1	Principle of multiple forging: setting and pull broaching along the first axis (a), (b), (c); setting and pull broaching along the second axis (d), (e), (f); setting and pull broaching along the third axis (g), (h), (i)	10
Figure 2.2	Principle of torsion under high pressure	12
Figure 2.3	Angles for equal channel angular pressing and ECAPed workpiece	13
Figure 2.4	Principles of ECA pressing: (a) $\Psi = 0^0$, (b) $\Psi = \pi - \Phi$, (c) Ψ is between $\Psi = 0^0$ and $\Psi = \pi - \Phi$	17
Figure 2.5	Route A: billet orientations	23
Figure 2.6	Shear plane orientation after four passes, $\Phi = 90^0$ route B _C	23
Figure 2.7	Shear strain planes for each ECAP routes for dies with (a) $\Phi = 90^0$ and (b) $\Phi = 120^0$	26
Figure 2.8	Orientation relationship between the grain elongation plane of the first pass and the shear plane of the second pass for ECAP route B _C or B _A . The angle between the grain elongation plane and the next shear plane is defined as θ	28
Figure 2.9	Shearing patterns for a die angle of $\Phi = 90^0$ and rotation around the X-axis: route B _C	30
Figure 2.10	Shearing patterns for a die angle of $\Phi = 120^0$ and rotation around the X-axis: route B _C	30
Figure 2.11	Schematic illustration of the ECAP process	36
Figure 2.12	Traces of deformed grids from the centre plane of the middle sections of billets that have been extruded halfway through a 120^0 die under conditions of: (a) low friction, (b) high friction, and (c) low friction with a 30 MPa back-pressure	38
Figure 2.13	Traces of deformed grids from the centre plane of the middle sections of billets that have been extruded halfway through a 90^0 die under conditions of: (a) low friction, (b) high friction.	38

Figure 2.14	Schematic representation of the progressive shearing of a material element as it travels through the die's deformation zone. 's' and 'n' refer to the streamline coordinate system used in the texture model and are tangential and normal to the streamlines, respectively	39
Figure 2.15	FEM predictions of deformation geometry changes during ECMAP	42
Figure 2.16	Schematic diagram of local microgalvanic cells created by silicon-containing cathodic impurities: (a) a case of non-ECAPed state and (b) a case of ECAPed state.	57
Figure 3.1	Sand and sodium silicate mixing	62
Figure 3.2	Pressing of mixed sand	63
Figure 3.3	Injection of CO ₂ gas and removing the mild steel bars	63
Figure 3.4	Mold ready for casting Al alloy	64
Figure 3.5	Annealing process for Al-Si-Mg alloy before ECAP	65
Figure 3.6	Workpieces shape (a) Cast workpiece ready for ECAP, (b) after one partial pass through die with $\Phi = 90^{\circ}$ and $\Psi = 20^{\circ}$, (c) after one pass through the die with $\Phi = 90^{\circ}$ and $\Psi = 20^{\circ}$	66
Figure 3.7	Die shapes; (a) die with $\Phi = 120$ and $\Psi = 0$, (b) die with $\Phi = 90$ and $\Psi = 0$ and (c) die with $\Phi = 90$ and $\Psi = 20$	68
Figure 3.8	The SEM system used in study	69
Figure 3.9	The reference directions in metallography examination and the planes designated X, Y and Z	70
Figure 3.10	The Future-Tech Vickers hardness tester FV	71
Figure 3.11	Sketch of pyramidal Vickers indentations on (a) X-plane, (b) Y-plane	72
Figure 3.12	Schematic representing the tension workpiece used in this study	73
Figure 3.13	The clamps of INSTRON machine, workpiece and its clamps	73
Figure 3.14	The Armfield Heat Conduction Apparatus	75
Figure 3.15	Corrosion test, (a) the Autolab system, (b) electrodes with polarization cell	76

Figure 4.1	Plasticine structure consists of four color balls as arranged	77
Figure 4.2	Microstructure of ECAPed plasticine through the die with $\Phi=120^0$ and $\Psi=0^0$ at: (a) 1 pass, (b) 3 passes, (c) 4 passes, (d) 8 passes, (e) 11 passes, and (f) 12 passes	79
Figure 4.3	The shear patterns of ECAPed plasticine through a die with $\Phi=120^0$ and $\Psi=0^0$ using route B_C after: (a) as arranged, (b) 1 pass, (c) 2 passes, (d) 3 passes, (e) 4 passes, (f) 5 passes	81
Figure 4.4	The shear patterns of ECAPed plasticine through a die with $\Phi=90^0$ and $\Psi=20^0$ using route B_C after: (a) as arranged, (b) one pass, (c) two passes, (d) three passes, (e) four passes, (f) five passes	83
Figure 4.5	SEM micrographs showing microstructures of the Al-Si-Mg alloy: (a) as cast (b) after 6 passes on the Y-plane.	85
Figure 4.6	The average values of Vickers microhardness (Hv) for the as cast and ECAPed Al-Si-Mg workpieces on X and Y planes with the number of passes through the die with $\Phi=120^0$ and $\Psi=0^0$	87
Figure 4.7	Vickers microhardness at X-plane for cast Al-Si-Mg alloy, 1, 3, 5 and 8 passes through the die with $\Phi=120^0$ and $\Psi=0^0$ from the bottom to the top of the workpiece	87
Figure 4.8	Vickers microhardness at Y-plane for cast Al-Si-Mg alloy, 1, 3, 5 and 8 passes through the die with $\Phi=120^0$ and $\Psi=0^0$ from the bottom to the top of the Workpiece	88
Figure 4.9	Vickers microhardness from the bottom to the top of the Al-Si-Mg workpiece at two locations for 8 passes through the die with $\Phi=120^0$ and $\Psi=0^0$ on the X and Y planes. {E: end of the workpiece}	88
Figure 4.10	Shows the temperature profile in heater, Al-Si-Mg workpiece and heat sink (a) as cast, (b) as cast after extrapolation, (c) at one pass, (d) as cast, 1, 5 and 8 passes through the die with $\Phi=120^0$ and $\Psi=0^0$	91
Figure 4.11	The thermal conductivity of the Al-Si-Mg alloy as a function of number of passes through the die with $\Phi=120^0$ and $\Psi=0^0$	92
Figure 4.12	Microstructures after ECAP using route B_C for (a) 2 passes at the top edge of the Al-Si-Mg workpiece for Y-plane, (b) 3 passes at Y-plane, (c) 4 passes at X-plane, (d) 7 passes at Y-plane.	94

Figure 4.13	Shows the Vickers microhardness (Hv) profiles at X-plane along the transverse distance from the bottom to the top surfaces of the cast, 2- 8 ECAPed Al-Si-Mg alloy workpieces through the die with $\Phi = 90^{\circ}$ and $\Psi = 20^{\circ}$	97
Figure 4.14	Shows the Vickers microhardness (Hv) profiles at Y-plane along transverse distance from the bottom to the top surfaces of the cast, 2, 3, 5 and 8 ECAPed Al-Si-Mg alloy workpieces through the die with $\Phi = 90^{\circ}$ and $\Psi = 20^{\circ}$	97
Figure 4.15	The average values of Vickers microhardness (Hv) for the As cast and ECAPed Al-Si-Mg workpieces at X & Y-planes with the number of passes through the die with $\Phi = 90^{\circ}$ and $\Psi = 20^{\circ}$	98
Figure 4.16	Shows the temperature profile in heater, Al-Si-Mg workpiece and heat sink (a): as cast after extrapolation (b): as cast and one pass, (c): as cast, 1, 5 and 8 passes	101
Figure 4.17	The thermal conductivity of the Al-Si-Mg alloy as a function of number of passes through the die with $\Phi = 90^{\circ}$ and $\Psi = 20^{\circ}$	102
Figure 4.18	Structure of annealed cast Al-Si-Mg alloy at 500 $^{\circ}$ C for 24h, magnification X 70 and the marker is 100 μ m	103
Figure 4.19	Microstructures of annealed cast Al-Si-Mg alloy at 500 $^{\circ}$ C for 24h ECAPed using route B _C die with $\Phi = 90^{\circ}$ and $\Psi = 0^{\circ}$ for (a) 1 pass in Y-plane, (b) 2 passes in X-plane, (c) 3 passes on Y-plane (d) six passes on X-plane	105
Figure 4.20	Shows the Vickers microhardness (Hv) profiles at X-plane along the transverse distance from the bottom to the top surfaces of the annealed cast Al-Si-Mg alloy, annealed cast alloy at 500 $^{\circ}$ C for 24h ECAPed to 1, 3, 5 and 8 passes through the die with $\Phi = 90^{\circ}$ and $\Psi = 0^{\circ}$	108
Figure 4.21	Shows the Vickers microhardness (Hv) profiles at Y-plane along the transverse distance from the bottom to the top surfaces of the annealed cast Al-Si-Mg alloy, annealed cast alloy at 500 $^{\circ}$ C for 24h ECAPed to 1, 3, 5 and 8 passes through the die with $\Phi = 90^{\circ}$ and $\Psi = 0^{\circ}$	108
Figure 4.22	Shows the average values of Vickers microhardness versus the number of passes for annealed Al-Si-Mg alloy workpieces at 500 $^{\circ}$ C for 24h through the die with $\Phi = 90^{\circ}$ and $\Psi = 0^{\circ}$ on X and Y-planes. (P:pass)	109

Figure 4.23	Temperature profile in the heater, Al-Si-Mg workpiece and heat sink for (a): as cast Al-Si-Mg alloy annealed at 500 °C for 24h, (b): as cast annealed and 1 pass, (c): as cast annealed, 1, 5, and 8 passes of Al-alloy workpieces through the die with $\Phi = 90^{\circ}$ and $\Psi = 0^{\circ}$	111
Figure 4.24	Shows thermal conductivity of the annealed Al-Si-Mg alloy at 500°C for 24h as a function of the number of passes through the die with $\Phi = 90^{\circ}$ and $\Psi = 0^{\circ}$	112
Figure 4.25	Structure of as annealed cast Al-Si-Mg alloy at 600 °C for 30 min, magnification X 70 and the marker is 100µm	113
Figure 4.26	Microstructures of cast and ECAPed Al-Si-Mg workpieces annealed at 600 °C for 30min at the first pass using route B _C followed by annealing at 230 °C for 20 min after 1 -3 passes and at 230 °C for 30 min after 7-8 passes (a) 2 pass on Y-plane, (b) 3 pass on Y- plane, (c) 7 passes on X-plane, (d) 8passes on X- plane.	115
Figure 4.27	Method of measuring the boundary misorientation angle, ϕ from selected area electron diffraction patterns.	118
Figure 4.28	The Vickers microhardness (Hv) profiles at X-plane along the transverse distance from the bottom to the top surfaces of annealed Al-Si-Mg alloy at 600 °C for 30min at the first pass followed by annealing at 230 °C for 20 min after 1 -3 passes and at 230 °C for 30 min after 7-8 passes using route B _C through the die with $\Phi = 90^{\circ}$ and $\Psi = 20^{\circ}$	119
Figure 4.29	The Vickers microhardness (Hv) profiles at Y-plane along the transverse distance from the bottom to the top surfaces of annealed Al-Si-Mg alloy at 600 °C for 30min at the first pass followed by annealing at 230 °C for 20 min after 1-3 passes and at 230 °C for 30 min after 7-8 passes using route B _C through the die with $\Phi = 90^{\circ}$ and $\Psi = 20^{\circ}$	120
Figure 4.30	The average values of Vickers microhardness versus the number of passes for annealed Al-Si-Mg alloy at 600 °C for 30min at the first pass followed by annealing at 230 °C for 20 min after 1 -3 passes and at 230 °C for 30 min after 7-8 passes using route B _C through the die with $\Phi = 90^{\circ}$ and $\Psi = 20^{\circ}$ on X and Y planes	120

Figure 4.31	Temperature profile in the heater, Al-Si-Mg workpiece and heat sink for annealed Al-Si-Mg alloy at 600 °C for 30min at the first pass followed by annealing at 230 °C for 20 min after 1 -3 passes and at 230 °C for 30 min after 7-8 passes (a) as cast Al-alloy annealed at 600 °C for 30min, (b) as annealed cast, 1, 2, 3, 7 and 8 passes of Al-alloy workpieces through the die with $\Phi = 90^{\circ}$ and $\Psi = 20^{\circ}$ using route B _C	123
Figure 4.32	Shows thermal conductivity of the annealed Al-Si-Mg alloy at 600°C for 30min as a function of the number of passes through the die with $\Phi = 90^{\circ}$ and $\Psi = 0^{\circ}$	124
Figure 4.33	Shows thermal conductivity of the Al-Si-Mg workpieces with the number of passes using the die with $\Phi = 120^{\circ}$, 90° and $\Psi = 0^{\circ}$, 20° at room temperature respectively, annealed workpieces at 500 °C for 24h before ECAP using the die with $\Phi = 90^{\circ}$ and $\Psi = 0^{\circ}$, and annealed workpieces at 600 C for 30 min using the die with $\Phi = 90^{\circ}$ and $\Psi = 20^{\circ}$	124
Figure 4.34	Tensile Al-Si-Mg workpieces tested to failure at room temperature: (a) as cast, (b) two passes, (c) three passes, (d) four passes, (e) five passes and (f) six passes	126
Figure 4.35	Tensile test to failure at room temperature of annealed Al-Si-Mg workpieces at 500 °C for 24h: (a) as annealed cast, (b) one pass, (c) two passes, (d) three passes, (e) four passes and (f) five passes	127
Figure 4.36	True stress-strain curves of Al-Si-Mg alloy at different number of passes through the die with $\Phi = 90^{\circ}$ and $\Psi = 0^{\circ}$	128
Figure 4.37	True stress-strain curves of annealed Al-Si-Mg alloy at 500 °C for 24h at different number of passes through the die with $\Phi = 90^{\circ}$ and $\Psi = 0^{\circ}$	129
Figure 4.38	The effect of number of passes on the maximum load of ECAP process for Al-Si-Mg alloy	129
Figure 4.39	The effect of the number of passes on the stress at the maximum load of ECAP process for Al-Si-Mg alloy	130
Figure 4.40	The effect of the number of passes on the % strain to failure of ECAPed Al-Si-Mg alloy through the die with $\Phi = 90^{\circ}$ and $\Psi = 0^{\circ}$	130
Figure 4.41	Scanning electron micrographs of the fracture surfaces of the tested Al-Si-Mg workpieces: (a) cast alloy, (b) after 3 passes, (c & d) after 5 passes with different magnification, and (e & f) after 6 passes with different magnification.	131

Figure 4.42	Scanning electron micrographs of the fracture surfaces of the tested annealed Al-Si-Mg workpieces at 500 °C for 24 hour: (a) annealed cast alloy, (b) after 2 passes, (c & d) after 3 passes with different magnification, and (e & f) after 4 passes with different magnification.	133
Figure 4.43	Schematic diagram showing the influence of shift in cathodic polarization curve on corrosion potential and corrosion current density.	135
Figure 4.44	Schematic diagram showing the influence of shift in anodic polarization curve on corrosion potential and corrosion current density.	136
Figure 4.45	Schematic diagram showing the influence of shift in cathodic polarization curve on corrosion potential and limiting current density.	136
Figure 4.46	Schematic diagram showing the influence of shift in cathodic and anodic polarization curves on corrosion potential and limiting current density.	137
Figure 4.47	Polarization curves of (a) cast Al-Si-Mg alloy and (b) ECAP with 7 passes through the die with $\Phi = 120^{\circ}$ and $\Psi = 0^{\circ}$.	140
Figure 4.48	SEM images of surface morphology with various number of passes of the ECAPed Al-Si-Mg alloy through $\Phi = 120^{\circ}$ and $\Psi = 0^{\circ}$ die after electrochemical test: (a) as cast alloy, (b) after 1 pass, (c) after 5 passes, and (d) after 8 passes	141
Figure 4.49	Polarization curves of (a) cast Al-Si-Mg alloy and (b) ECAPed with 7 passes through a die with $\Phi = 90^{\circ}$ and $\Psi = 20^{\circ}$.	143
Figure 4.50	SEM images of surface morphology with various number of passes of the ECAPed Al-Si-Mg alloy through $\Phi = 90^{\circ}$ and $\Psi = 20^{\circ}$ die after electrochemical test: (a) as cast alloy, (b) after 2 passes, (c) after 5 passes, and (d) after 8 passes	144
Figure 4.51	Polarization curves of (a) cast annealed Al-Si-Mg alloy at 500 °C for 24 h, and (b) ECAPed annealed with 7 passes through a die with $\Phi = 90^{\circ}$ and $\Psi = 0^{\circ}$.	146
Figure 4.52	SEM images of surface morphology with various number of passes of the ECAPed annealed Al-Si-Mg alloy at 500°C for 24 h through $\Phi = 90^{\circ}$ and $\Psi = 0^{\circ}$ die after electrochemical test: (a) as annealed cast alloy, (b) after 2 pass, (c) after 5 passes, and (d) after 8 passes	147

- Figure 4.53 Polarization curves of (a) cast annealed Al-Si-Mg alloy at 600 °C for 30min, and (b) ECAPed with 7 passes through the die with $\Phi = 90^\circ$ and $\Psi = 20^\circ$ annealed at 230 °C for 30 min 150
- Figure 4.54 SEM images of surface morphology with various number of passes of the ECAPed annealed Al-Si-Mg alloy at 600°C for 30 min through $\Phi = 90^\circ$ and $\Psi = 20^\circ$ die after electrochemical test: (a) as annealed cast alloy at 600 °C for 30 min, (b) after 1 pass and (c) after 3 passes at 230 °C for 20 min, and (d) after 8 passes at 230 °C for 30 min. 151
- Figure 4.55 EDS spectra and SEM morphology of impurities present at the surface of corroded ECAPed (after one pass) annealed Al-Si-Mg alloy at 500 °C for 24 h: (a and a[#]) at wide area, (b and b[#]) at small area 153

LIST OF SYMBOLS

A	Area
φ	Boundary Misorientation Angle
σ	Electrical conductivity
e^-	Electron
σ_0	friction stress
d	Grain Size
N	Number of passes
k_y	positive constant of yielding
γ	Shear strain
γ_{SFE}	Stacking Fault Energy
ε_N	Strain accumulated after N passes
Q	The amount of heat
β	The angle between grain elongation direction and the extrusion axis
θ	The angle between the grain elongation plane and the next shear plane is defined
Ψ	The angle defining the outer arc of curvature at the point of intersection of the two channels
k_e	The electronic component of thermal conductivity
ε_{eq}	The equivalent strain
Φ	the internal angle between the two intersecting channels
k_l	The lattice component of thermal conductivity
ΔT	The temperature gradient
k	Thermal conductivity

Hv	Vickers microhardness
σ_y	Yield tress
μm	Micrometer
T_m	The Melting Temperature
b_a	Anodic Tafel slop
b_b	Cathodic Tafel slop
i	current density(A/m^2)
P	Load
T	Temperature in Kelvin
t	Time
Z	Atomic mass

LIST OF ABBREVIATIONS

aq	Aqueous
ECAP	Equal Channel Angular Pressing
EDS	Energy Dispersive X-ray
F.C.C.	Face Centered Cubic
FEM	Finite Element Method
HAGB	High Angle Grains Boundary
HPT	High Pressure Torsion
LAGB	Low Angle Grain Boundary
MF	Multiple Forging
PDZ	Plastic Deformation Zone
PP	Elastic-perfectly Plastic
Route A	The sample is not rotate between consecutive pressings
Route B _A	The sample is rotate by 90 ⁰ in alternate directions between consecutive pressings
Route B _C	The sample is rotate by 90 ⁰ in the same direction between consecutive pressings
Route C	The sample is rotate by 180 ⁰ between consecutive pressings
SAED	Selected Area Electron Diffraction
SEM	Scanning Electron Microscopy
SH	Strain Hardening
SPD	Severe Plastic Deformation
TEM	Transmission Electron Microscopy
UFG	Ultra Fine Grains
UTM	Universal testing machine

LIST OF PUBLICATIONS

1. Ali A. Aljubouri, Luay B. Hussain, Nurulakmal Mod Sharif and M.Z. Abdullah, "The Influence of Plastic Deformation via ECAP on the Hardness of 6061 Al alloy". Paper presented at International Conference on Recent Advances in Mechanical & Materials Engineering (ICRAMME 2005), session 15, No. 67, 30-31 May 2005, Ungku Aziz Hall, University of Malaya, Kuala Lumpur, Malaysia.
2. Ali A. Aljubouri, Luay B. Hussain, Nurulakmal Mod Sharif and M.Z. Abdullah, "Enhancement of Al – 1.3 Si Alloy Properties by ECAP Method". Paper presented at 14th Scientific Conference & 15th Annual General Meeting of Electron Microscopy Society of Malaysia, PP. 8-15, 5th – 7th December 2005, Vistana Hotel, Penang.
3. Ali A. Aljubouri, Luay B. Hussain, Nurulakmal Mod Sharif and M.Z. Abdullah, "Effect Annealing on Some Mechanical and Physical Properties of Al Alloy Processed by ECAP" Poster presented at 14th Scientific Conference & 15th Annual General Meeting of Electron Microscopy Society of Malaysia, PP 131-139, 5th – 7th December 2005, Vistana Hotel, Penang.
4. Ali A. Aljubouri, Luay B. Hussain, Nurulakmal Mod Sharif, " The Effect of ECAP on the Hardness and Structure of Al alloy". Poster presented at the 6th Field – Wise Seminar for Materials Engineering on Biomaterials, Nanomaterials, Advanced Materials & Composites, held at School of Materials and Mineral Resources Engineering, University Sains Malaysia, on 17th May 2005.
5. Luay B. Hussain, Ali A. Aljubouri, M.A.M. Jebri, Nurulakmal Mod Sharif, "Spot Welding Copper 1%Cr Electrode Tips Produced via Equal Channel Angular Pressing". Paper to be published in a Journal of the ASEAN Committee on Science & Technology. Sent for Referee.

KESAN SUDUT PENEKANAN SALUR BERSUDUT SAMA TERHADAP MIKROSTRUKTUR DAN SIFAT-SIFAT ALOI Al-Si-Mg.

ABSTRAK

Penyelidikan ini bertujuan untuk meningkatkan sifat-sifat fizikal dan mekanikal aloi Al-Si-Mg melalui penghalusan struktur ira yang dihasilkan oleh kecacatan plastik lampau. Struktur ini diperolehi secara penekanan sudut salur sama (*equal channel angular pressing* (ECAP)). AloI ini mempunyai komposisi (dalam % berat) 1.3 Si, 0.3 Mg, 0.18 Fe, 0.023 Cu, 0.019 Mn, 0.017 Zn, 0.014 Ga, 0.011 Ti dan selebihnya Al. Dalam proses ECAP sampel ditekan melalui dai bersudut 90° dan 120° menggunakan laluan B_C . Sampel diputar 90° dalam arah yang sama diantara setiap urutan penekanan melalui dai ECAP. Sampel mengalami kecacatan plastic secara ricihan tulen semasa melalui sudut persimpangan. Penilaian mikrostruktur, sifat fizikal dan sifat mekanikal sampel Al-Si-Mg yang tersempit melalui proses ECAP dianalisis menggunakan mikroskop imbasan electron (SEM), ujian kekerasan mikro Vickers, ujian tegangan, ujian konduksi terma serta ujian elektrokimia kakisan. Kesan-kesan sudut penekanan, terhadap sifat-sifat mekanikal dan penghalusan mikrostruktur pada suhu sepuh lindap, (230°C dan 500°C) dan suhu ubah bentuk (600°C) telah dinilai. Dari pada pemerhatian perkemangan mikrostruktur proses ECAP menghasilkan pengurangan saiz butir daripada 70-100 μm kepada sekitar 200 nm. Sampel selepas ECAP yang melalui proses sepuh lindap pada 500°C selama 24 jam sebelum ECAP juga mempamerkan butir-butir dengan saiz serupa. Manapun walaubagai proses sepuh lindap pada 230°C selama 20-30 minit selepas ECAP membawa kepada peningkatan saiz butir kepada 300 hingga 600 nm. Kekerasan mikro ditingkatkan sebanyak 250-300 % dan terdapat sedikit penurunan di dalam nilai yang di perolehi apabila masa sepuh

lindap ke atas sampel ECAP ditingkatkan. Kekonduksian terma bertambah sebanyak 19-30%, bergantung kepada sudut salur dan suhu sepuh lindap. Nilai yang lebih tinggi diperolehi untuk sudut yang lebih tirus dan suhu sepuh lindap lebih tinggi. Kekuatan tegangan sampel tuangan Al-Si-Mg dikaji selepas melalui ECAP dengan sudut salur 90° . Kekuatan tegangan mutlak, beban maksimum dan pemanjangan meningkat dengan bertambahnya bilangan ulangan proses ECAP. Keputusan yang diperolehi dari ujian kakisan menunjukkan sampel Al-Si-Mg yang telah melalui proses ECAP mempunyai rintangan kakisan yang lebih baik dalam 3.5% NaCl berbanding sampel Al-Si-Mg yang dituang. Kadar kakisan berkurang apabila proses ECAP diulang untuk sampel yang sama tetapi kadar kakisan bertambah dengan peningkatan suhu sepuh lindap. Sifat-sifat benda kerja yang dikaji menunjukkan perubahan yang jelas selepas melalui laluan pertama proses ECAP. Adalah diketahui bahawa, proses ECAP merupakan proses yang mudah, murah dan berkesan untuk menambahbaik sifat-sifat fizikal dan mekanikal aloi Al-Si-Mg. Peningkatan sifat fizikal dan mekanikal ini menawarkan potensi yang baik untuk di gunakan di dalam pelbagai aplikasi industri.

THE INFLUENCE OF EQUAL CHANNEL ANGULAR PRESSING ANGLES ON THE MICROSTRUCTURE AND PROPERTIES OF Al-Si-Mg ALLOY

ABSTRACT

The aim of this research is to improve the physical and mechanical properties of Al-Si-Mg alloy by grain structure refinement produced by severe plastic deformation through equal channel angular pressing (ECAP). This alloy has a composition (in wt. %) of 1.3 Si, 0.3 Mg, 0.18 Fe, 0.023 Cu, 0.019 Mn, 0.017 Zn, and 0.014 Ga, 0.011 Ti balance Al. In ECAP process, the workpieces are pressed through a 120° and 90° dies using route B_C. Through this route the sample is rotated by 90° in the same direction between each consecutive pressing through the ECAP dies. Workpieces undergo plastic deformation by pure shear through the intersecting corner. Microstructure evaluation, physical and mechanical properties of the extruded Al-Si-Mg workpieces by equal channel angular pressing were conducted using scanning electron microscopy (SEM), micro-Vickers hardness tester, tensile test machine, heat conduction apparatus and auto lab corrosion test system. The effect of die angles on the microstructural refinement and mechanical properties at annealing temperature (230 °C and 500 °C) and deformation temperature (600 °C) were investigated. From the microstructure evolution, ECAPed resulted in reduction of grain size from 70-100 μm to about 200nm. The ECAPed workpieces that underwent annealing at 500 °C for 24h before ECAP also displayed grains with similar sizes. However, annealing process at 230 °C for 20-30min after ECAP leads to an increase of grain size to around 300 to 600nm. Microhardness was improved by 250-300% and there was slight reduction in its value obtained with

the increase in annealing time of ECAPed workpieces. The enhancement of thermal conductivity is by 19-30%, depending on channel angle and annealing conditions. It showed higher value for sharper channel angle (90°), and higher annealing temperature. From the tensile tests, the maximum load, maximum stress and elongation to failure increases with the number of passes through the ECAP die. Results from the corrosion experiments of deformed Al-Si-Mg alloy in 3.5% NaCl solution showed better corrosion resistance compared to as-cast Al-Si-Mg alloy. The corrosion rate was reduced with the number of passes through the ECAP dies but its value increases with increasing annealing temperature. In general, a drastic change in all investigated mechanical and physical properties occurred after the first pass through the ECAP dies. It is well known that the ECAP provides a simple, cheap and effective processing technique for producing nanostructured Al-Si-Mg alloy. Consequently the improvement in the mechanical and physical properties offers great potential to be used in various industrial applications.

.

CHAPTER ONE

INTRODUCTION

It is well known that there are significant advantages to be gained from deforming metallic alloys to very high plastic strains. These include microstructural refinement (Segal, 1995) and enhanced mechanical properties (Valiev et al., 1993 and Markushev et al., 1997).

In conventional processes, like gas condensation (Sanders et al., 1997; Glieter, 1989), ball milling with subsequent consolidation (Koch and Cho, 1992; Eckert et al., 1992; Kock, 1997) and rolling (Philippe, 1994) one or more of the material dimensions are continuously being reduced with strain, can only be achieved in foils or filaments, which have few structural applications. In other words, it is possible to use these methods for producing ultrafine grain structure even to the size of nanometer, but it is not easy to use these methods to produce large bulk workpieces, which then limits the industrial applications. The inert gas submicrocrystalline process is capable of producing small crystallites with a narrow size distribution. Mean grain size is controlled by operation temperature and the inert gas pressure. The powder produced is compacted in vacuum to form samples. Besides, nanocrystalline materials can also be synthesized by high energy ball milling of elemental, intermetallic compound, or immiscible powders (Jang and Kock, 1990). However, it should be pointed out that the residual porosity in compacted samples and impurities from ball milling would not be easily eliminated, and the mechanical and

physical properties inherent to various nanostructured materials are influenced by these imperfections (Valiev et al., 1992).

Recent investigations have shown that severe plastic deformation (SPD) is an effective method for forming submicron grain material (Segal, 2002; Yu et al., 2005). Three requirements should be taken into account while developing methods of severe plastic deformation (SPD) for production of nanostructures in bulk workpieces. Firstly, it is essential to obtain submicrometer grain structures with high angle grain boundaries. Secondly, to achieve stable properties of the processed materials, the nanostructures must be uniform within the whole volume of the workpiece. Thirdly, the workpiece should not have any mechanical cracks or damage when it is exposed to large plastic deformation. Traditional methods can not meet these requirements (Valiev et al., 2000).

Different techniques have been used to introduce large quantities of plastic strain into metals. Rolling is the most conventional technique, but higher strain levels (greater or equal to 10) have been achieved more recently for example by torsion under high pressure (Valiev, 1993; Gertsman et al., 1994; Alexandrov et al., 1998), by cycle's extrusion (Korbel and Richert, 1985), or by a specific method involving simple shear inside a localized zone called equal channel angular pressing (ECAP) (Iwahashi et al., 1996; Segal, 1995).

ECAP, invented by Segal et al., (1981) in the beginning of the 1980s, has been the subject of intensive study in recent years due to its capability of producing large full density samples containing an ultrafine (or nanometer

scale) grain size by repeating the process while maintaining the original cross-section of the workpiece.

Processing by ECAP involves pressing a sample through a die within a channel that is bent into an L-shaped configuration. In general, the equivalent strain is close to ~ 1 when the two parts of the channels intersect at 90° (Iwahashi et al., 1996). There are many parameters that affect the microstructural evolution in materials. Among them are, the die angle, which determines the strain introduced in the material for each deformation pass (Iwahashi et al., 1996; Nakashima et al., 1998; Luis Perez, 2004), and the number of passes through the die, which corresponds to the total accumulated strain applied to the workpiece. The deformation route, which involves rotating the workpiece between each successive passes, is another important parameter in microstructure development (Furukawa et al., 1998; Iwahashi et al., 1997 and 1998a). In addition, the content of impurities (Iwahashi et al., 1998b), pressing speed (Berbon et al., 1999), the deformation temperature Cao et al., 2003; Zheng et al., 2006), and the friction between the die walls and the workpiece are also essential parameters (Semiatin et al., 2000; Oruganti et al., 2005).

However, different microstructures can be developed in ECAP by rotating the workpiece between extrusion cycles (Iwahashi et al., 1997, 1998a, 1998c). It is possible to define four distinct processing routes A, B_A, B_C and C, which are classified by how the workpiece is rotated with respect to the die for each subsequent pass. When the workpiece is rotated after each pass around its

longitudinal axis through the angles: 0° (route A), $\pm 90^{\circ}$ (route B_A), $+ 90^{\circ}$ (route B_C), and $+180^{\circ}$ (route C).

The SPD techniques may form grains with sizes in the order of 100-200 nm and with high angle grain boundaries (Valiev et al., 2000). The SPD materials should be described as nanocrystalline, since they often have a mean grain size of about 20-100 nm. Several articles have reported that the deformation structure of most alloys processed by ECAP at room temperature exhibit homogeneous equiaxed grains with a high fraction of high angle grain boundaries (65%) (Sun et al., 2002).

Many ultrafine-grain aluminum alloys have been produced by ECA pressing and attractive mechanical properties such as high strength and superplasticity have been reported from ECAPed aluminum alloys (Wang and Prangnell, 2002; M-Morris et al., 2003; May et al., 2005). Several recent steps have been taken to evaluate the overall potential of the ECAP process. First, it was shown that ECAP processing may be scaled up relatively easily to produce large bulk materials having properties similar to those achieved in small-scale laboratory investigations (Horita et al., 2001). Second, various procedures were developed to simplify the procedure for imposing high total strains including the use of a multi-pass pressing facility (Nakashima et al., 2000) and by adopting alternative devices such as a rotary die (Ma et al., 2005). Third, there have been recent attempts to incorporate the ECAP process into conventional cold rolling for the continuous production of metal strip (Han et al., 2004). In general,

the major advantage of an ECAP process is that it is relatively cheap and is arguably less complex than the other SPD processes.

In the present study, ECAP with different die angles was used to deform the material and obtain ultrafine grained structure. The present work has many objectives. The first is to advance our understanding of the deformation mechanism in ECAP, and investigate the effect of some parameters that affect the microstructure evolution such as die angles and thermal annealing for the Al-Si-Mg alloy. Second, to estimate the mechanical properties such as the refinement of grains, microhardness and tensile strength of the Al alloy subjected to significant grain refinement and strengthened through ECAP. Third, to study the possibility to enhance the thermal conductivity and corrosion resistance through consecutive passes of Al alloy during the ECAP die. The characterization of ultrafine grain structure mainly relies on scanning electron microscopy (SEM).

CHAPTER TWO

LITERATURE SURVEY

2.1 Aluminum and Aluminum Alloys

Aluminum is the second most plentiful metal on earth, but until the late 1800s, was expensive and difficult to produce because Al_2O_3 can not be reduced by heating it with coke. Development of electrical power and the Hall (in the USA)-Heroult (in France) process for electrolytically reducing Al_2O_3 to liquid metal allowed aluminum to become one of the most widely used and inexpensive materials.

2.1.1 Aluminum and Aluminum Alloys Properties

The development of applications for Al and Al alloys can be attributed to several of their properties which include:

- **Lightness:** Aluminum is one of light metals. Its density is $2700 \text{ kg}\cdot\text{m}^{-3}$, or one third the density of steel. The strength of some Al alloys comparable to that of mild carbon steel can approach 700MPa. This indicates that the strength of these alloys is higher by 30 times than that of pure aluminum. This combination of high strength and lightness makes aluminum well suited to transportation vehicles such as ships, aircraft, rockets, trucks, automobiles, along with portable structures such as ladders, scaffolding, and gangways. (Donald, 2001).
- **Corrosion resistance:** Aluminum has an excellent resistance to corrosion , it reacts with oxygen very rapidly even at room temperature to produce a thin

but very dense film of oxide (Al_2O_3) which forms on the metal surface to protect the underlying metal from many corrosive environments and quickly reform when damaged.

- Thermal conductivity: An excellent thermal conductivity for aluminum makes it very suitable for heating and cooling applications such as for the manufacture of domestic cooking utensils, automobile radiators, refrigerator evaporator coils and heat exchangers. (Higgins, 1997)
- High electrical conductivity: The electrical conductivity is around two third of copper but it conducts twice electricity as an equal weight of copper, therefore aluminum is an ideal for use in electrical transmission cables. Aluminum bars and tubes are widely used in connecting stations for high and medium voltage outdoor networks.
- Reflectivity: Aluminum is an excellent reflector of radiant energy such as heat and lamp reflectors.
- High toughness at cryogenic temperature: At low temperature has a higher strength and toughness, making it useful for cryogenic vessels.
- Nontoxic: Because aluminum and any corrosion product which are formed are nontoxic, aluminum is used in the packaging of food and sweets, cooking utensils and vessels in food processing.
- The ease of fabrication: Aluminum is easy to form and fabricate by various processes such as extruding, bending, drawing forging casting, rolling and machining.
- The ease of use: Specific tools not necessary to process aluminum alloys and they lend themselves to joining techniques such as welding, bolting, riveting, clinching, adhesive bonding, and brazing (Martin, 2004).

- The diversity of aluminum alloys: There are eight or nine series of aluminum alloys which give a very wide range of compositions, properties and uses (James, 2004).
- Recyclability: Aluminum made from recycled material requires only 5% of the energy needed to produce aluminum from bauxite which contains aluminum oxide. The recycling rate of end of life aluminum is roughly; (Martin, 2004).
 - 85% in the building industry and public amenities
 - 80% in the transport sector,
 - 70% in mechanical and electrical engineering, and
 - 65% in house hold application.

2.1.2 Aluminum Series

Aluminum alloys are classified into two categories, wrought alloys, those that are worked to shape, and cast alloys, those that are poured in a molten state into a mold that determines their shape. The diversity of alloys and the wide range of certain properties explain the growth in applications from aeronautics to packaging. All aluminum products belong to one of eight alloy series listed in appendix A (James, 2004 and Martin, 2004).

2.2 Severe Plastic Deformation (SPD) Techniques

It is well established that three axis forging, high pressure torsion straining (HPT) and equal channel angular pressing (ECAP) are known methods of providing large plastic deformation. However, the last two methods are the most well known processes used to reduce the grains in polycrystalline materials to submicrometer or nanometer level (Valiev et al., 1991). These procedures are capable of producing large samples without the presence of residual porosity for a wide range of industrial application. This advantage gives these techniques super priority over other methods for preparing materials with submicrostructure grain sizes. The deformation imposed during both processes introduces a high dislocation density into the deformed workpieces and this leads to arrays of grains which are highly deformed and having grain boundaries which tend to be poorly defined and tend to be curved or wavy (Valiev et al., 1993 and Wang et al., 1993).

2.2.1 Multiple Forging (MF)

This method is one of the nanostructure creation methods in rather brittle materials because processing starts at elevated temperatures and specific loads on tooling are low. The principle of this method is shown in Figure 2.1. It assumes multiple repeats of free forging operations, setting drawing with a change of the axis of the applied strain load. The efficiency of this technique to provide homogeneous strain is less than that of the torsion straining and ECAP. Multiple forging was used for microstructural refinement in many materials and alloys, such as pure Ti, Ti alloys, Ni alloys (Salishchev et al., 1994), and others.

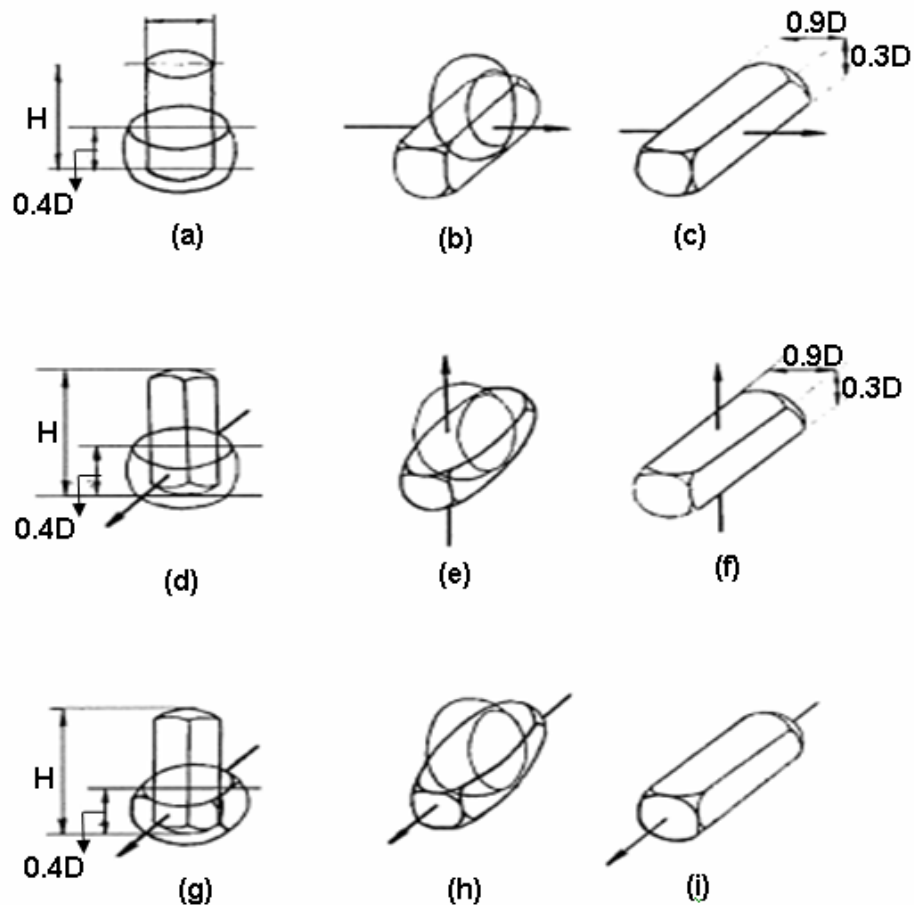


Fig. 2.1: Principle of multiple forging: setting and pull broaching along the first axis (a), (b), (c); setting and pull broaching along the second axis (d), (e), (f); setting and pull broaching along the third axis (g), (h), (i) (Valiev et al., 2000).

2.2.2 High Pressure Torsion (HPT)

The high pressure torsion process is capable of forming uniform nanostructures having smaller grain sizes than other severe plastic deformation methods; also it is able to introduce continuously variable magnitudes of deformation, thus the microstructure evolution studies are attainable. An important change in the microstructure is noticed after deformation by half rotation, but to obtain homogenous nanostructure several rotations are required (Valiev, 1997). HPT has two advantages: (i) it is capable to produce small grain sizes, often in the nanometer range $\sim 100\text{nm}$ (ii) providing a capability for processing brittle materials such as intermetallic and semiconductors

(Languillaume et al., 1993 and Islamgaliev et al., 1994) and the disadvantage of HPT is that the workpieces fabricated by this technique are usually of a disk shape not exceeding 20 mm in diameter and 1 mm in thickness (Lowe and Valiev, 2000). Also, the precise deformation conditions and constraints during HPT may vary since they depend on friction between the rotating anvil and the workpiece.

Submicrocrystalline and nanocrystalline structures may be obtained by torsion using the Bridgman technique (Bridgman, 1952) where the deformation occurs by torsion of the workpiece under high pressure. In this process the workpiece is subjected to large plastic deformation by torsion where the workpiece is held between anvils and strained in torsion under applied pressure of several GPa as shown in Figure 2.2. A lower holder rotates and surface friction forces deform the workpiece by shear. After several rotations the deformation by the given mode often results in similar refinement of a microstructure in the center of the workpieces as well the processed nanostructure is usually homogeneous at the radius of samples. This homogeneity has been confirmed by the uniform distribution of microhardness values across the test workpieces section. The strain imposed in the workpiece is given by: (Valiev, 1997)

$$\gamma = \frac{2\pi RN}{l} \dots\dots\dots 2.1$$

Where, N is the number of rotations, R is the distance from the axis of the disk and *l* is the thickness of the workpiece. Two points can be concluded from the above formula; (i) the strain value should change linearly from zero in the center of the workpiece to the maximum value at the end of its diameter; (ii) during deformation the initial thickness of the workpiece is reduced by approximately

50% under high compression pressure. Two forms of torsional deformation of thin disks have been described. The first, due to Bridgman, comprises simultaneous compression and torsion of a disk which is not constrained laterally, therefore; its diameter is free to expand beyond that of the tooling anvils (Bridgman, 1935). The second one is a comprise compression /torsional deformation of a disk situated between a tight fitting cylindrical plunger and die, a geometry which prevents lateral expansion of the workpiece (Valiev et al., 1997a). The torsional technique is used with more or less success in the laboratory since it does not fully meet the requirements of commercial technologies. Therefore; Bridgman's technique is applicable for obtaining nanocrystalline structure in thin foil form workpieces.

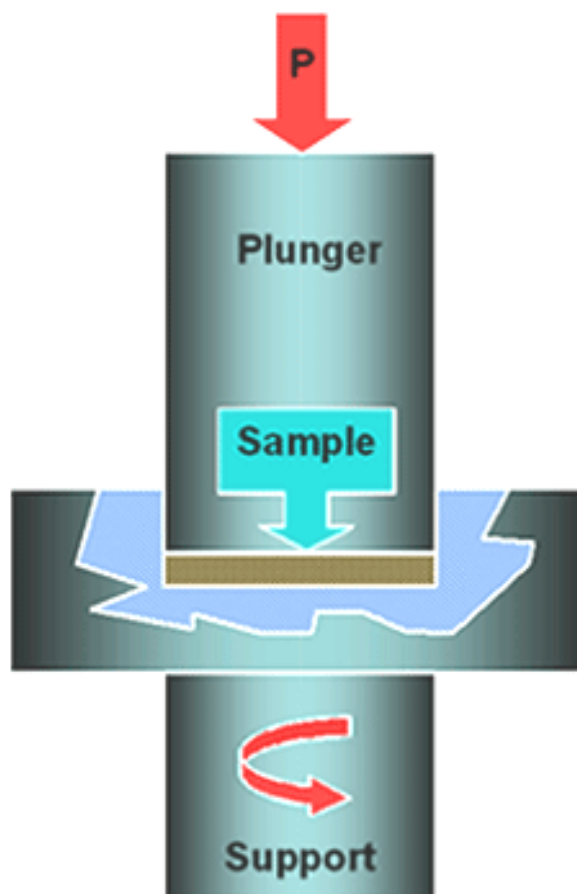


Fig. 2.2: Principle of torsion under high pressure.

2.2.3 Equal Channel Angular Pressing (ECAP)

Equal channel angular pressing is one of the most promising processes that can produce ultrafine grained materials through the process of simple shear by pressing a workpiece through a die with two intersecting channels, equal in cross section as shown in Figure 2.3 (Iwahashi et al., 1996). Various techniques are used to analyze the microstructure development of Al alloys, for example, (Iwahashi et al., 1997) used transmission electron microscopy (TEM) with selected area electron diffraction (SAED) to observe the microstructure of Al material. While (Gholinia et al., 2000) used high resolution electron backscattered diffraction to quantitatively measure the misorientation of boundary. Many researchers used Scanning electron microscopy (SEM) for testing the shape and size of the grains.

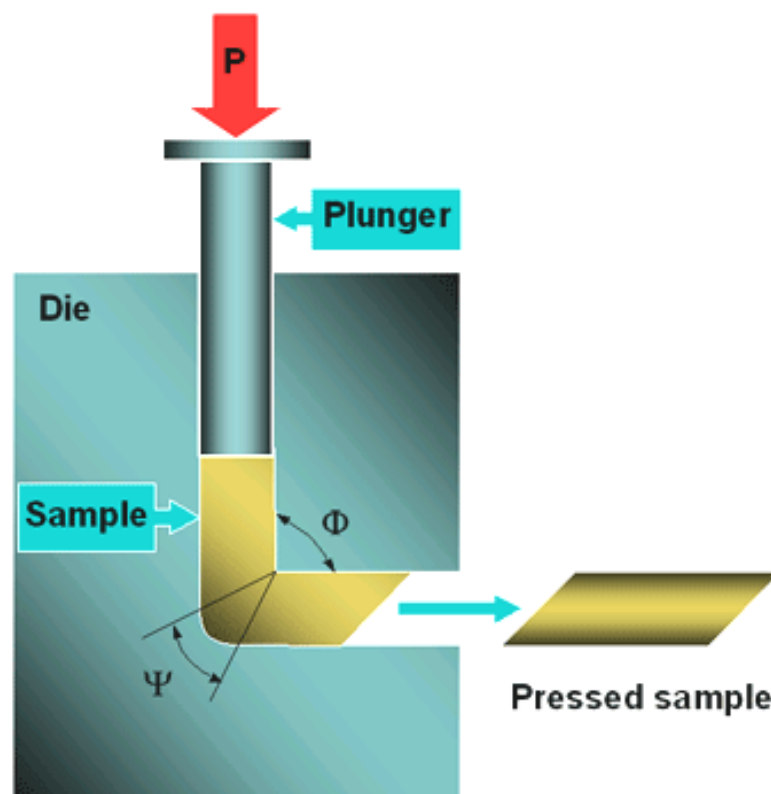


Fig. 2.3: Angles for equal channel angular pressing and ECAPed workpiece.

ECAP has many advantages comparing with other severe plastic deformation processes;

- ECAP may be used to attain a microstructure where it is possible to achieve superplastic forming at very high strain rates.
- ECAP is being applicable producing a deformation with no change in the cross sectional dimensions of the workpiece on passage through the die.
- ECAP may be readily scaled up for the production of relatively large bulk workpieces that may be suitable for use in industrial applications.
- There have been new developments in utilizing the ECAP method including using a rotary die or multipass facility in order to achieve high strains without removing the workpiece from the ECAP die.
- Deformation in ECAP occurs at the shear plane, which is lying at the intersection of the two channels. Therefore; the deformation in the ECAP processed workpiece is very localized and homogenous in the localized deformation zone.
- ECAP has been combined with other metal working process to provide a more versatile procedure.

2.3 Principle of ECAP

The principle of ECAP is shown schematically in Figure 2.4, where two equal cross section channels intersected at two angles, Φ is the internal angle between the two intersecting channels and Ψ is the angle defining the outer arc of curvature at the point of intersection of the two channels. Figures 2.4(a) and (b) correspond to the limiting conditions of $\Psi = 0$ and $\Psi = \pi - \Phi$, respectively,

and Figure 2.4(c) corresponds to an intermediate situation where Ψ lies at an arbitrary angle between $\Psi = 0$ and $\Psi = \pi - \Phi$.

In Figure 2.4(a) where $\Psi = 0$, a small element in the workpiece, initially square in cross section with dimensions given by $abcd$, becomes deformed by shear on passage through the die into the configuration given by a',b',c',d' . Using the notation in Figure 2.4(a), it follows that the shear strain, γ is given by:

$a'q \perp qd'$, where

$$qd' = ad, \text{ and } ab' = dc' = a'p = pq = ad \cot(\Phi/2)$$

so that,

$$a'q = 2ad \cot(\Phi/2).$$

Therefore, for the condition where $\Psi = 0$,

$$\gamma = 2 \cot(\Phi/2) \dots\dots\dots 2.2$$

In Figure 2.1(b) where $\Psi = \pi - \Phi$, the shear strain is given by

$\gamma = rc' \perp rb'$, where

$$rb' = da = (oa - od) \text{ and}$$

$$ab' = dc' = oa \Psi = (rc' + od \Psi) \text{ so that,}$$

$$rc' = (oa - od) \Psi.$$

Therefore, for this condition,

$$\gamma = \Psi \dots\dots\dots 2.3$$

In Figure 2.4(c) where Ψ represents an intermediate situation, the shear strain is:

$\gamma = a'u \perp d'u$ where

$$d'u = ad \text{ and } a'u \text{ may be obtained from the relationships}$$

$$a'u = (a't + tu) = (rc' + as),$$

$$as = ad \cot\left(\frac{\Phi}{2} + \frac{\Psi}{2}\right),$$

$$ab' = dc' = (as + os \Psi) = rc' + od \Psi, \text{ then}$$

$$rc' = (os - od) \Psi + as,$$

$$\therefore a'u = (os - od) \Psi + 2as,$$

$$\therefore (os - od) = ad \operatorname{cosec}\left(\frac{\Phi}{2} + \frac{\Psi}{2}\right), \text{ so that}$$

$$a'u = 2ad \cot\left(\frac{\Phi}{2} + \frac{\Psi}{2}\right) + ad \Psi \operatorname{cosec}\left(\frac{\Phi}{2} + \frac{\Psi}{2}\right).$$

Therefore, the shear strain for this intermediate condition is given by

$$\gamma = 2 \cot\left(\frac{\Phi}{2} + \frac{\Psi}{2}\right) + \Psi \operatorname{cosec}\left(\frac{\Phi}{2} + \frac{\Psi}{2}\right) \dots\dots\dots 2.4$$

When $\Psi = 0$, equation (2.4) reduces to equation (2.2) and to equation (2.3)

when

$$\Psi = \pi - \Phi.$$

The equivalent strain, ε_{eq} is represented by

$$\varepsilon_{eq} = \left[\frac{2 \left[\varepsilon_x^2 + \varepsilon_y^2 + \varepsilon_z^2 + \frac{\gamma_{xy}^2 + \gamma_{yz}^2 + \gamma_{zx}^2}{2} \right]}{3} \right]^{1/2} \dots\dots\dots 2.5$$

so that the strain ε , after one cycle is

$$\varepsilon = \left[\frac{2 \cot\left(\frac{\Phi}{2} + \frac{\Psi}{2}\right) + \Psi \operatorname{cosec}\left(\frac{\Phi}{2} + \frac{\Psi}{2}\right)}{\sqrt{3}} \right] \dots\dots\dots 2.6$$

Since in each passage through the die the same strain is accumulated, the following equation represent a more general relationship allowing one to calculate the strain value of the workpiece during ECAP for N passes.

$$\varepsilon_N = N \left[\frac{2 \cot\left(\frac{\Phi}{2} + \frac{\Psi}{2}\right) + \Psi \operatorname{cosec}\left(\frac{\Phi}{2} + \frac{\Psi}{2}\right)}{\sqrt{3}} \right] \dots\dots\dots 2.7$$

During ECAP the direction and the number of workpiece passes through die are very important for microstructure refinement.

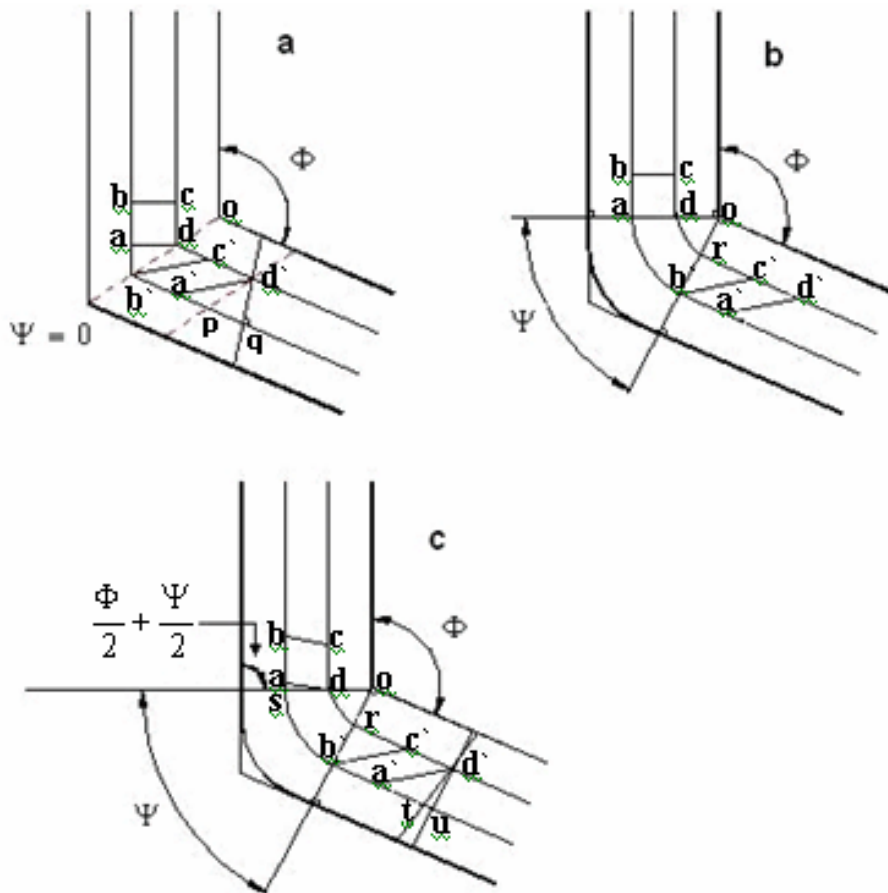


Fig. 2.4: Principles of ECA pressing: (a) $\Psi = 0^\circ$, (b) $\Psi = \pi - \Phi$, (c) Ψ is between $\Psi = 0^\circ$ and $\Psi = \pi - \Phi$ (Iwahashi et al., 1996).

2.4 Estimations of the Strain in ECAP

The strain imposed on the workpiece in ECAP depends upon the two angles defined in Figure 2.4, Φ and Ψ . Segal (1995) showed that the strain accumulated after N cycles through the die is given by:

$$\varepsilon_N = \frac{2N}{\sqrt{3}} \cot \frac{\Phi}{2} \dots\dots\dots 2.8$$

The above equation was also derived by (Utyashev et al., 1996).

Iwahashi et al., (1996) obtained equation 2.7 which including the influence of the geometric process parameters of the die such as Φ and Ψ angles.

It is apparent that equation 2.7 reduces to equation 2.8 when $\Psi = 0^\circ$. According to equation 2.7, the magnitude of the equivalent strain depends upon the values of Φ and Ψ angles, where it decreases with increasing of both angles. The equivalent strain during ECAP can decrease from the maximum of 1.15 at minimum value of $\Psi = 0^\circ$ to the minimum of 0.907 at the maximum value of $\Psi = 90^\circ$, when channel angle is fixed as $\Phi = 90^\circ$. The channel angle Φ has more influence on the strain generated during ECAP than the die corner angle Ψ (Prangnell et al., 1997); (Delo and Semiatin, 1999); (Semiatin et al., 2000). Wu and Baker (1997) reported good agreement with equation 2.7 in model experiments where workpieces were extruded through Plexiglas die. Measurements of the shear strain from single and multipass extrusions showed that the center of the workpieces (away from the die wall) did indeed undergo deformations which were well predicted by equation 2.7. However, the workpiece regions near the die wall underwent substantially lower strains due to sticking friction. In order to avoid a reduction in the cross-sectional dimensions of the workpiece as it passes through the die, there is a maximum value of the

arc angle, Ψ_{\max} , given by $(\pi - \Phi)$ (Iwahashi et al., 1996). At the maximum value, Ψ_{\max} ,

$$\varepsilon_N = \frac{N(\pi - \Phi)}{\sqrt{3}} = \frac{N\Psi_{\max}}{\sqrt{3}} \dots\dots\dots 2.9$$

2.5 Microstructure Evolution

The microstructure develops as a natural consequence of the evolution of the deformed state, therefore; the meaning of submicron or nanocrystalline grain structure is not immediately apparent after using severe plastic deformation processing. A severely deformed alloy with an average grain size less than $1 \mu\text{m}$ may still contain many low angle grain boundaries and the grains can be highly elongated in the deformation direction (Bowen et al., 2000a). The definition proposed here is; the average grain size of high angle grain boundaries (boundaries misorientated by $> 15^\circ$) must be less than $1 \mu\text{m}$, or 100 nm in all orientations and, the proportion of high angle grain boundary (HAGB) area must be $> 70\%$ relative to the total boundary area in the material. This proportion of HAGB is required to produce a stable grain structure and is suggested on the basis that it has been shown, experimentally (Gholinia et al., 2000) and theoretically (Humphreys et al., 1999).

2.5.1 Mechanism of Microstructural Evolution during ECAP

2.5.1(a) Grains Subdivision

A very numerous increase in the HAGB area within a material is required to form a submicron grain structure. During ECAP at low temperature less than $0.5 T_m$, where T_m is a material melting temperature, new HAGB area can be created by two main mechanisms that operate simultaneously; (i) the extension of pre existing boundaries in proportion to the applied strain (Gill Sevillano et al., 1980) and (ii) the generation of new HAGBs formed by grains subdividing (Hughes and Hansen, 1997). The general principals of new HAGBs formed by grain subdivision using route B_C are summarized bellow:

- The first pass through the die divides the large grains into arrays of subgrains that are well delineated; these subgrains are elongated and lie in bands structure. The selected area electron diffraction (SAED) patterns consist of discrete diffraction spots showing that the grain boundaries have low angles of misorientation.
- A second pass through the die, following a rotation by 90° in the same sense between passes, leads to microstructure, where the subgrain structure has broken into an array of ultrafine grains .This breaking up of the subgrain bands is due primarily to the development of a second set of bands. SAED shows some spreading of the diffraction spots, so that the misorientations across the boundaries between neighboring grains have increased with increasing strain.

- After three passes, there is no longer any evidence for the initial formation of the subgrain bands, the microstructure consists of an essentially equiaxed array of grains. The SAED patterns exhibit diffracted beams scattered around rings, this indicating that some of the grain boundaries have high angles of misorientation.
- After the fourth passes, there is now an equiaxed array of grains on each of the three orthogonal planes of sectioning. There is no evidence for the earlier formation of subgrain bands, and the SAED patterns consist of rings of diffraction spots showing that the grain boundaries have high angle of misorientation on each plane of sectioning. (Nakashima et al., 1998; Iwahashi et al., 1997; Iwahashi et al., 1998c).

Segal, (1999) explained the effectiveness of producing an ultrafine grained structure by the intersection of shear bands. Two conditions to optimize the ECAP were improvement; (i) ECAP should provide uniform and intensive simple shear at each pass and (ii) develop of high angle grain boundaries during multipass processing. Condition (i) is performed using a die with $\Phi = 90^\circ$ and $\Psi = 0^\circ$ under frictionless condition. During the first pass, coarse grains are subdivided by shear bands with a large portion of high angle grain boundaries. During the following passes new groups of shear bands are induced while the first pass groups remain stable and change their orientations thus defining various networks of high angle boundaries for different routes.

For route A, as shown in Figure 2.5 the shear plane for the second pass is perpendicular to the shear plane at the first pass, and the shear bands

formed in the second pass intersects the workpiece axis at an angle of 45° , while the shear bands created in the first pass changes orientation on angle of about 20° to the workpiece axis. Intersection of the first pass shear bands with the following passes groups subdivide the structure for subgrains elongated along the flow direction.

With route C, the shear plane is retained at any pass. Beyond the first pass the shear bands boundaries are saturated by dislocations. During the following passes, for further strain accommodation, another mechanism including subdivision of shear bands for equiform subgrains and their progressive rotation (Nesterenko et al., 1997).

With route B_C , the shear plane orientation changed with the number of passes, as shown in Figure 2.6, intersection of these shear planes develop an approximate uniform network into the material. Therefore, an equiaxial and ultrafine structures with high angle grain boundaries are attained for rout B_C with lowest number of passes. Thus, route B_C is more effective than routes C and A, and it is more suitable for grain refinement (Segal, 1999). Other researchers Chakkingal et al., (1998); Shin et al., (2000) have studied the microstructure evolution, and they noticed that the misorientation between subgrains increases and some of these subgrains will become grains with HAGBs with increasing number of ECAP passes.

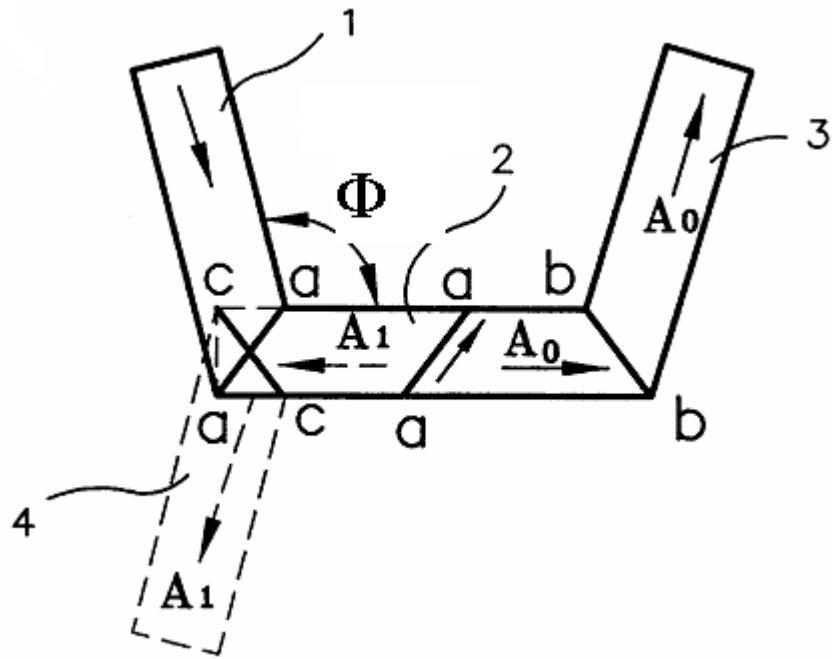


Fig. 2.5 Route A: billet orientations; (Segal, 1999).

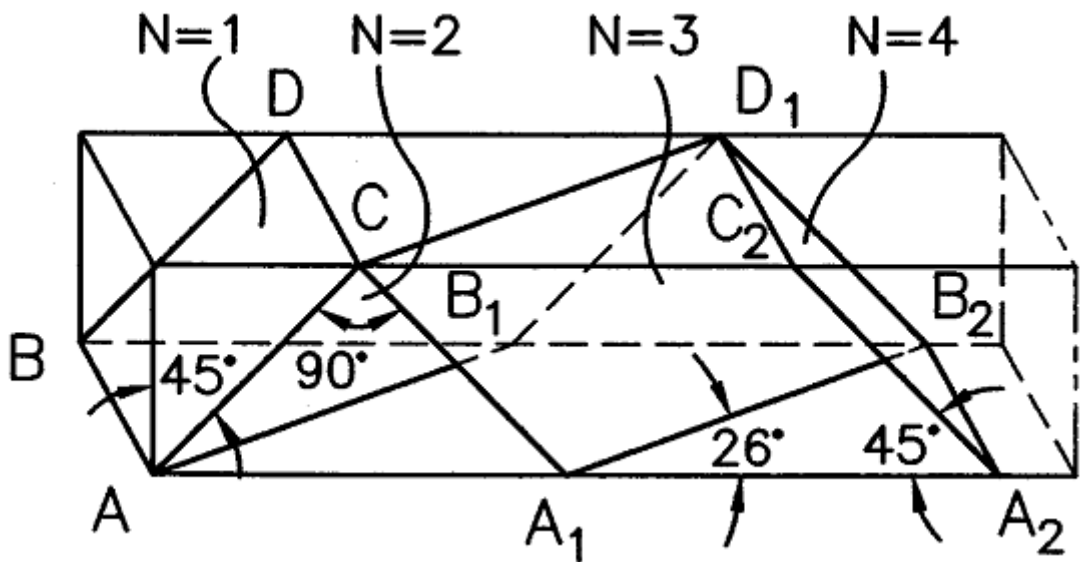


Fig. 2.6 Shear plane orientation after four passes, $\Phi = 90^\circ$ route B_C (Segal, 1999).

According to Iwahashi et al. (1998a) investigation, in route B_C with a 90° die angle, the shearing planes intersect at 120° . As a result of this duality in shearing directions, subgrain bands are developed on repetitive pressing along two separate and intersecting sets of planes, and this leads to a reasonably equiaxed array of high angle grain boundaries HAGBs. In route A, the shear planes intersect at an angle of 90° and route C keep the same orientation. Therefore it was inferred that route B_C is the preferable procedure for use in ECAP experiments. Iwahashi et al. (1997) established that the effectiveness of producing fine grained structure is in the order of $C > A$, because route C permits the shear to build continuously on a single set of planes, whereas in route A the extent of shearing is divided equally between two sets of orthogonal planes.

Prangnell et al. (2000) deformed an Al–3% Mg–0.2% Zr–0.2% Fe alloy using a die with Φ angle 120° with all four ECAP routes. They found that route A is the most effective route in producing grain refinement and HAGBs, because it does not produce redundant strain. In route B_C , the next odd pass reverse the strain from the previous odd pass and the next even pass reverse the strain from the previous even pass, therefore route B_C is less effective than route A in refining the grain size. While in route C the shear strain from the even pass reverse the strain from the previous odd pass, therefore creating redundant strain making it least effective in refining grains. Oh-Ishi et al. (1998) processed pure Al using a die with $\Phi = 90^\circ$ and they found that $B_C > B_A$. Furukawa et al. (1998) explain these experimental observations through studying the deformation of cubic workpieces processed with each ECAP routes. They inferred that the effectiveness of the routes is $B_C > C > A \approx B_A$.

because the cubic workpiece is restored after $4N$ and $2N$ passes (N is integer) in routes B_C and C respectively. Meanwhile route A and B_A deformed the workpiece continuously.

2.5.1(b) Shearing Planes

The grain refinement created by ECAP procedure mainly depends on macroscopic shearing patterns, because ECAP involves simple shear deformation by pressing a workpiece through the shear plane of the die.

Iwahashi et al. (1998a, c); Nemoto et al. (1999), considered the angles between the shearing strain planes of repetitive passes from each ECAP route. However; they failed to explain the effect of these shearing planes on the grain refinement. The grain refinement under repetitive passes with varying shear planes promoted the consideration of accumulative strain (Prangnell et al., 2000). Figure 2.7 shows shear strain planes for each ECAP route with $\Phi = 90^\circ$ and 120° (Zhu and Lowe, 2000). Where the most effectively grains refining of face centered cubic (F.C.C.) materials like pure Al or Al alloys, occurs when α (the angle between two adjacent shear strain planes) equal to 60° . This value of α reported for both routes A and B_C from a $\Phi = 120^\circ$ die and a $\Phi = 90^\circ$ die respectively. Thus, they succeeded to explain why route A from a $\Phi = 120^\circ$ die and route B_C from a $\Phi = 90^\circ$ die have been most effective in refining the grain size. But they failed to interpret why route B_C is more effective than route B_A for a $\Phi = 90^\circ$ die, since both routes have the same value of α and B_A has no redundant strain which make it more effective than route B_C in grain refinement.